Check for updates

Metal–organic framework derived hollow porous CuO–CuCo₂O₄ dodecahedrons as a cathode catalyst for Li–O₂ batteries†

Shu-ying Zhen,[a] Hai-tao Wu,[b] Yan Wang,[b] Na Li,[a] Hao-sen Chen,*[a] Wei-li Song, [ID] [a] Zhen-hua Wang,[b] Wang Sun*[b] and Ke-ning Sun [ID] *[b]

Herein, hollow porous CuO–CuCo₂O₄ dodecahedrons are synthesized by using a simple self-sacrificial metal–organic framework (MOF) template, which resulted in dodecahedron morphology with hierarchically porous architecture. When evaluated as a cathodic electrocatalyst in lithium–oxygen batteries, the CuO–CuCo₂O₄ composite exhibits a significantly enhanced electrochemical performance, delivering an initial capacity of 6844 mA h g⁻¹ with a remarkably decreased discharge/charge overpotential to 1.15 V (*vs.* Li/Li⁺) at a current density of 100 mA g⁻¹ and showing excellent cyclic stability up to 111 charge/discharge cycles under a cut-off capacity of 1000 mA h g⁻¹ at 400 mA g⁻¹. The outstanding electrochemical performance of CuO–CuCo₂O₄ composite can be owing to the intrinsic catalytic activity, unique porous structure and the presence of substantial electrocatalytic sites. The *ex situ* XRD and SEM are also carried out to reveal the charge/discharge behavior and demonstrate the excellent reversibility of the CuO–CuCo₂O₄ based electrode.

1. Introduction

Eco-friendly and high-efficiency energy storage devices, with enhanced energy and power densities, have garnered significant research attention due to the rapidly growing demand for electronic devices and electric vehicles and increasing environmental concerns.[1,2] Among the current secondary battery systems, non-aqueous rechargeable Li–O₂ batteries (LOBs) render a compelling theoretical specific gravimetric energy density of ∼3500 W h kg⁻¹, which exhibits their promise in future energy storage devices.[3–5] Nevertheless, several practical issues, including high over-potential, inferior reversibility and poor rate performance, hinder the successful realization of LOBs. Most of these shortcomings arise from the sluggish reaction kinetics, involving a tri-phase interface (electrode/oxygen/electrolyte), and the passivation of cathode by insoluble and insulating Li₂O₂ product.[6–8] Therefore, various cathode electrocatalysts, such as heteroatom-doped carbonaceous materials, precious metals and their alloys, transition metal oxides and carbides,

have been designed to boost the oxygen reduction reaction (ORR) and oxygen evolution reaction (OER) processes, reduce the over-potential, increase the rate performance and enhance the stability of LOBs.[9–11] The transition metal oxides, in general, and copper–cobalt complex oxides, in particular, exhibit promise as cathode catalysts for LOBs due to their low cost, controllable structure and high bifunctional activity.[12–15]

Besides, the porous architecture of the air electrode also has a crucial effect on the electrochemical performance of LOBs.[5,10,13] The air electrode surface is easily passivated by insoluble and insulating discharge products, *i.e.*, Li₂O₂, which hinders the efficient transfer of reactants and electrons and adversely influences the reaction kinetics. Hence, the deliverable capacity and energy density of LOBs are much lower than the theoretical. Therefore, the hierarchical porous structure is required to efficiently transfer the reactants/electrons and store the discharge products (Li₂O₂), which results in improved capacity and rate capability of LOBs.[15,16]

In recent years, nano-scale metal–organic frameworks (MOFs) have been employed as promising precursors to fabricate transition metal oxides with desirable pore structure.[17–19] For instance, Zhang *et al.* have fabricated MOFs derived porous Co–Mn–O nanocubes and employed as cathode catalysts for LOBs to obtain improved rate capability and cyclic performance, which can be ascribed to the synergistic effect of porous architecture and electrocatalytic activity.[20] Recently, hierarchically porous ZnO/ZnFe₂O₄/C nanocages have been synthesized by using octahedral Fe(III)-

[a]Institute of Advanced Structure Technology, Beijing Institute of Technology, 100081, Beijing, China. E-mail: chenhs@bit.edu.cn; Fax: +86-010-68918696; Tel: +86-010-68918696

[b]Beijing Key Laboratory for Chemical Power Source and Green Catalysis, School of Chemistry and Chemical Engineering, Beijing Institute of Technology, Beijing, 100081, China . E-mail: sunwang@bit.edu.cn; bitkeningsun@163.com

† Electronic supplementary information (ESI) available. See DOI: 10.1039/c9ra02860a

MOF-5, as a template, and utilized as a cathodic material in LOBs.[21] MOF-derived transition metal oxides render several unique traits, such as hierarchically porous architecture, abundant interconnected channels, a large surface area and pore volume, which are very desirable for efficient cathode catalysts in LOBs.[20–22] However, to the best of our knowledge, the fabrication and investigation of MOF-derived hierarchically porous copper–cobalt oxide nanocatalysts for LOBs are less reported.

Herein, hollow CuO–CuCo$_2$O$_4$ dodecahedron nanostructure, with hierarchical meso- and macro-pores, has been synthesized by a simple solvothermal method, where zeolitic imidazolate framework-67 (ZIF-67) has been employed as the self-sacrificing template. The electrochemical performance of hollow CuO–CuCo$_2$O$_4$ dodecahedron nanoparticles has been studied as an air electrode catalyst for LOBs. The hierarchically-arranged surface mesopores and hollow macropores facilitate the oxygen diffusion and electron transport and relieve pore blockage due to the accumulation of the discharge products, i.e., Li$_2$O$_2$. Combined with the high bifunctional catalytic activity of copper–cobalt composite oxide, the LOBs with CuO–CuCo$_2$O$_4$ based air-electrode achieved a high capacity of 6844 mA h g^{-1} at 100 mA g^{-1}, exhibited low over-potential and rendered superior reversibility, which implies that the MOF-derived cathode catalyst is a highly promising alternative for next-generation LOBs.

2.   Experimental section

2.1   Materials

2-Methylimidazole (98%), cobaltous nitrate hexahydrate (AR, 99%, Co(NO$_3$)$_2$·6H$_2$O), cupric nitrate trihydrate (AR, 99%, Cu(NO$_3$)$_2$·3H$_2$O), and anhydrous methanol (AR, 99.5%) were purchased from Aladdin. Ultrapure water with a resistivity of 18.25 MΩ cm was prepared in laboratory. All raw materials were used as received without further purification.

2.2   Materials synthesis

ZIF-67 preparation. 4 mmol of Co(NO$_3$)$_2$·6H$_2$O and 16 mmol of 2-methylimidazole were added into 50 mL of anhydrous methanol and stirred at room temperature, respectively. A purple-colored mixture solution can be obtained after quickly adding the 2-methylimidazole solution to the cobalt solution. Then the mixture solution was stirred at room temperature for 40 min and subsequently aged for 24 h. In the end, the mixture solution was centrifuged and the resulting purple-colored precipitate was washed by anhydrous methanol and dried under vacuum at 80 °C for 12 h.

CuO–CuCo$_2$O$_4$ preparation. 160 mg of ZIF-67 was added into 100 mL of anhydrous methanol with 0.5 mmol Cu(NO$_3$)$_2$·3H$_2$O and 1 mmol Co(NO$_3$)$_2$·6H$_2$O, followed by stirring in a water bath at 70 °C for 40 min. Then, Cu–Co hydroxide was obtained by centrifugation and vacuum-dried at 80 °C for 12 h. The hollow CuO–CuCo$_2$O$_4$ composite has been achieved by heat treating the copper–cobalt hydroxide at 400 °C for 1 h in air.

2.3   Material characterization

X-ray diffraction (XRD) patterns of ZIF-67 and CuO–CuCo$_2$O$_4$ composites were obtained by using an X'Pert PRO MPD X-ray diffractometer with Cu Kα radiations. Moreover, the discharged/charged cathode electrodes without washing treatment had been enwrapped in a thin polyimide film to reduce their exposure to the air during the XRD characterization. The morphology and microstructure of CuO–CuCo$_2$O$_4$ composites have been investigated by scanning electron microscopy (SEM, Quanta FEG 250) and transmission electron microscopy (TEM, JEM-2001F). The high-resolution TEM (HRTEM) images were obtained by JEM-2010F, equipped with energy dispersive X-ray spectroscopy (EDXS). The discharged/charged cathode electrodes were washed by tetraethylene glycol dimethyl ether (TEGDME) (99%, Sigma) solvents and dried in argon-filled glove box before SEM characterization. The electrode samples were hermetically sealed during transfer to the electron microscope. X-ray photoelectron spectroscopy (XPS) was carried out by using Physical Electronics 5400 ESCA. The surface area and pore structure were determined by N$_2$ adsorption/desorption isotherms, which have been recorded by an Autosorb-IQ2-MP-C instrument.

2.4   LOBs fabrication and electrochemical characterization

The air electrode slurry was fabricated by blending 40 wt% CuO–CuCo$_2$O$_4$ composite, 50 wt% Super P and 10 wt% polytetrafluoroethylene (PTFE) in isopropanol. Then, the homogeneously mixed slurry was sprayed on carbon paper and vacuum-dried at 100 °C for 24 h. The loading of the active material was ∼0.4 mg cm^{-2}. Then, a coin-cell battery, with uniformly distributed holes on the cathode side, has been assembled in an argon-filled glove box to investigate the electrochemical performance of CuO–CuCo$_2$O$_4$ composite in LOBs. The coin-cell battery consists of an oxygen electrode, a glass fiber separator (Whatman, GF/D) and a lithium metal anode. The Li metal had been immersed in 0.1 M LiClO$_4$–propylene carbonate electrolyte for several days before being used. 1 M LiClO$_4$/DMSO were used as the electrolyte. LAND CT2001A system was used to record the galvanostatic discharge/charge curves in the voltage range of 2.2–4.5 V (vs. Li$^+$/Li) under a pure oxygen atmosphere (>99.999%, Beijing Beiwen Gas Manufacturing Factory). Cyclic voltammetry (CV) was carried out by using CHI660E electrochemical workstation in the voltage range of 2.0–4.5 V (vs. Li$^+$/Li) at a scan rate of 0.1 mV s^{-1}.

3.   Results and discussion

As depicted in Fig. 1, dodecahedral ZIF-67 nanoparticles were first synthesized and further used as a self-sacrificing template to prepare CuCo layered dihydroxides with hollow dodecahedron morphology. After calcination at 400 °C with a heating rate of 1 °C min^{-1} in air, hollow CuO–CuCo$_2$O$_4$ dodecahedron with hierarchical porous structure was fabricated.

The SEM and TEM images of ZIF-67 particles exhibit a uniform particle size of ∼700 nm and a solid dodecahedral structure, as given in Fig. S1.† The XRD pattern of the prepared
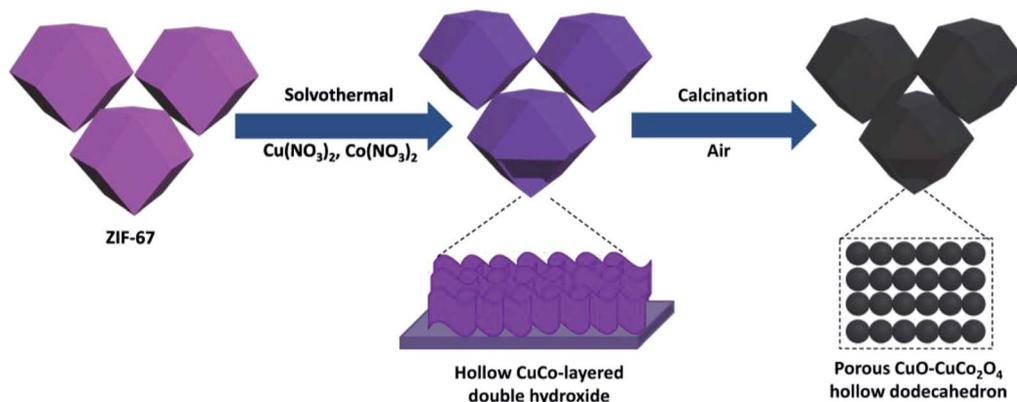
Fig. 1 Schematic of the fabrication process of the hollow porous CuO–CuCo$_2$O$_4$ dodecahedron.

ZIF-67 demonstrates excellent crystallinity and consistency with the simulated pattern (Fig. S2†). Due to the hydrolysis of Cu(NO$_3$)$_2$ and Co(NO$_3$)$_2$ in anhydrous methanol under solvothermal conditions, Cu–Co hydroxide has been formed due to the co-precipitation of Co^{3+} ions released by slowly dissolved ZIF-67 and Cu^{2+}/Co^{3+} ions in the solvent.[23] As revealed by SEM and TEM images (Fig. 2), ZIF-67 derived flower-like Cu–Co hydroxide precursor, assembled by ultrathin nanosheets, presents a hollow structure and maintains the dodecahedral morphology. Interestingly, there are one or more large openings on the surface of each Cu–Co hydroxide dodecahedron, which are supposed to facilitate the rapid diffusion of oxygen molecules and improve utilization and reaction rate of the internal surface.[24,25]

After calcination in air, Cu–Co hydroxide has been transformed into CuO–CuCo$_2$O$_4$ composite. As shown in Fig. 3a, XRD patterns demonstrate the presence of cubic CuCo$_2$O$_4$ (JCPDS no. 76-1887) and hexagonal CuO (JCPDS no. 43-1003). SEM images (Fig. 3b and S3a†) reveal that CuO–CuCo$_2$O$_4$ composites maintained the hollow dodecahedral structure with a small number of surface openings, which exhibited a decrease in size (∼500 nm) after calcination. TEM images (Fig. 3c) further confirmed the hollow-porous structure of CuO–CuCo$_2$O$_4$ composites and exhibited that the surface nanosheets are actually comprised of nanocrystals, with an average diameter of ∼10 nm (inset in Fig. 3c). The N$_2$ adsorption–desorption isotherms of CuO–CuCo$_2$O$_4$ composites present type-IV curves, with a distinct H3-type hysteresis loop in the middle-to-high
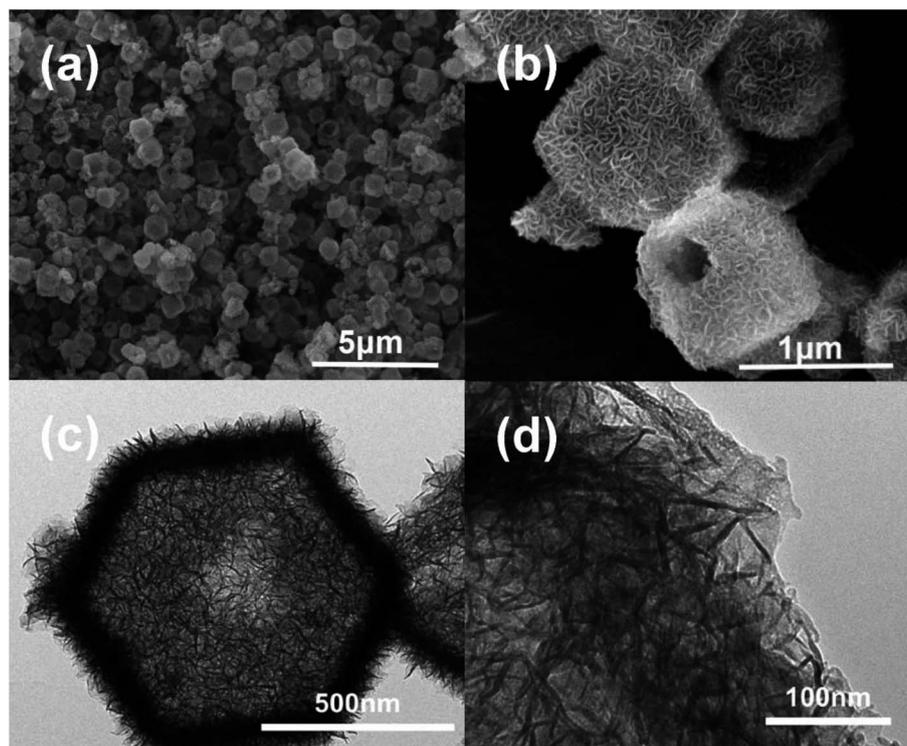

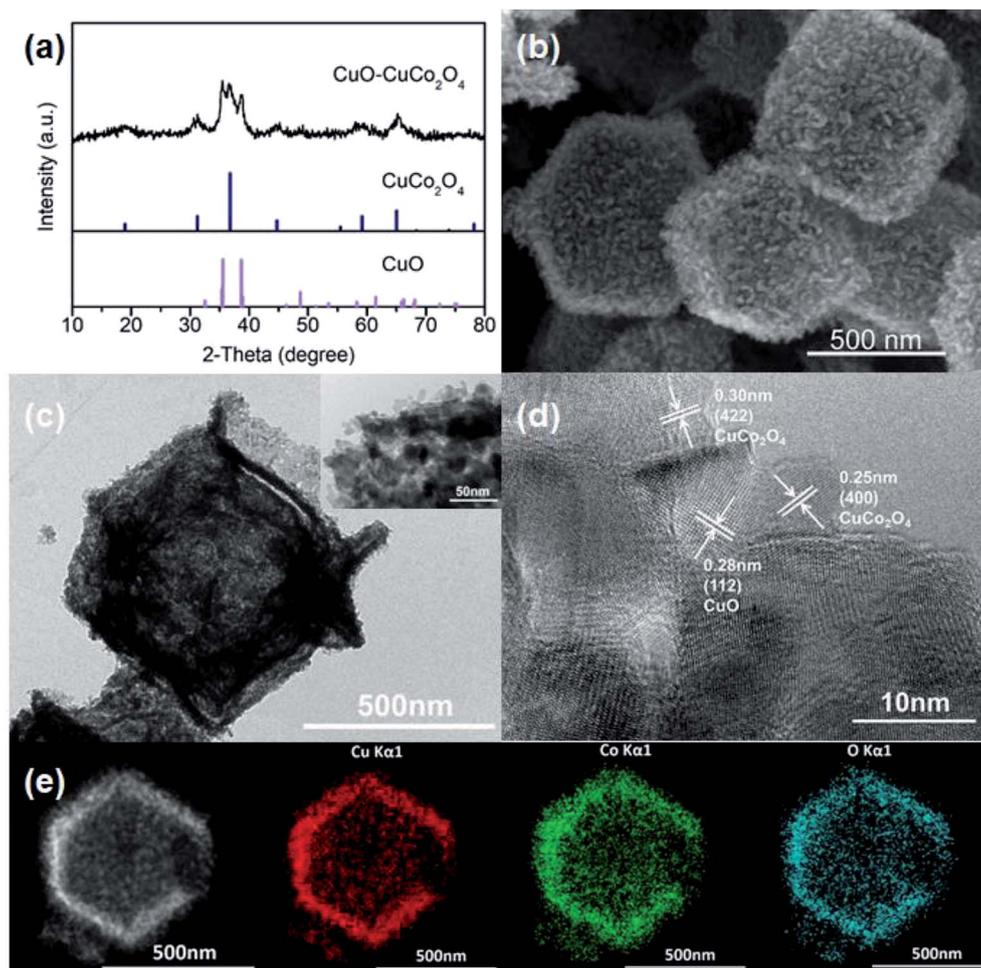**Fig. 2** SEM (a and b) and TEM (c and d) images of the Cu–Co hydroxide precursor.

Fig. 3 Materials characterization: (a) XRD pattern, (b) SEM image, (c) TEM image, (d) HRTEM image and (e) elemental maps of CuO–CuCo$_2$O$_4$ composites.

pressure region, which confirms the presence of mesopores. The porous CuO–CuCo$_2$O$_4$ composites render a high surface area of 124 m^2 g^{-1}, with the main pore size of 3–12 nm (Fig. S4†).

Fig. 3d presents the HRTEM image of CuO–CuCo$_2$O$_4$ composite, where the lattice spacing of 0.25 and 0.30 nm belongs to (400) and (422) diffraction planes of CuCo$_2$O$_4$, respectively, and 0.28 nm represents the (112) plane of CuO. One should note that these observations are consistent with XRD results. The selected area electron diffraction (SAED, Fig. S3b†) pattern also confirms the polycrystalline feature of the CuO/CuCo$_2$O$_4$ composite. Furthermore, the elemental mapping results (Fig. 3e) indicate the uniform distribution of Cu, Co, and O in CuO–CuCo$_2$O$_4$ composite. The contrast in element distribution between the edge and the center also confirms the hollow structure and the existence of few large surface openings in CuO–CuCo$_2$O$_4$ dodecahedron.

Fig. 4a presents the wide-range XPS spectrum of CuO–CuCo$_2$O$_4$ composites, indicating the presence of Cu, Co, and O elements.[15] The high-resolution XPS spectrum of Cu 2p is depicted in Fig. 4b, revealing the co-existence of Cu$^+$ and Cu^{2+} ions.[15,26] The Cu 2p$_{3/2}$ spectrum consists of two peaks at 932.7

and 935.3 eV, corresponding to tetrahedral Cu$^+$ and Cu^{2+} ions, respectively, and one main peak at 933.9 eV, which can be assigned to octahedral Cu^{2+}.[26,27] Moreover, the binding energies of 940.8 and 943.3 eV in the Cu 2p spectrum correspond to the satellites of divalent Cu.[26,27] Furthermore, both peaks of Co 2p$_{3/2}$ spectrum (Fig. 4c) can be fitted with two spin–orbit doublets at the binding energies of 779.2 and 780.4 eV, corresponding to the octahedral Co^{3+} and tetrahedral Co^{2+} ions, respectively.[15,27] The peaks at 781.8 and 789.1 eV can be ascribed to the satellites of Co^{2+} ions.[27] The peak of Co 2p$_{1/2}$ spectrum can be decomposed into two peaks, centered at 794.3 and 795.8 eV, corresponding to octahedral Co^{3+} and tetrahedral Co^{2+} ions, respectively.[27,28] In O 1s spectrum (Fig. 4d), the binding energy of 529.4 eV belongs to lattice oxygen (O^{2-}) and the peak at 531.1 eV represents the defects, chemisorbed oxygen and coordinated lattice oxygen.[15,26] These results reveal the existence of abundant surface valence states and defects, which can improve the intrinsic catalytic activity of the CuO–CuCo$_2$O$_4$ composite.

To evaluate the electrochemical performance of CuO–CuCo$_2$O$_4$ composites, the LOBs with CuO–CuCo$_2$O$_4$ composite and pure Super P cathodes are fabricated and evaluated by
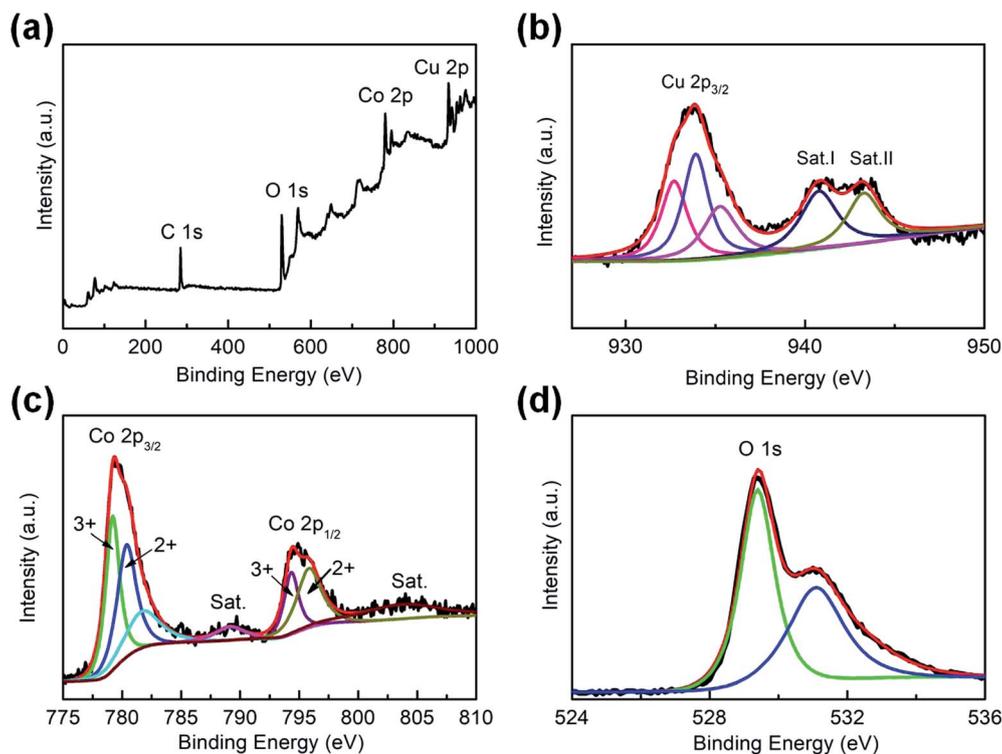
Fig. 4 Materials characterization: XPS spectra of CuO–CuCo$_2$O$_4$: (a) full spectrum, high-resolution XPS spectrum of (b) Cu 2p, (c) Co 2p, and (d) O 1s.

using cyclic voltammetry (CV) and galvanostatic charge/discharge tests. Fig. 5a presents the CV curves of CuO–CuCo$_2$O$_4$ composites and pure Super P cathodes. It can be readily observed that CuO–CuCo$_2$O$_4$ composites exhibited a higher reduction peak potential of 2.55 V and a lower oxidation peak potential of 3.75 V. Moreover, the reduction and oxidation current densities of the CuO–CuCo$_2$O$_4$-based LOBs were larger than the pure Super P-based LOBs, which indicates the superior catalytic activity of CuO–CuCo$_2$O$_4$ for ORR and OER.[22,27] The abundant octahedral Cu^{2+} ions in CuO–CuCo$_2$O$_4$ composite, as illustrated in Fig. 4b, may explain its excellent OER activity. It has been reported that the octahedral divalent ions render superior catalytic activity toward OER than the tetrahedral ions.[15,26]

Hence, the CuO–CuCo$_2$O$_4$ composite is a promising air electrode material in LOBs owing to its excellent catalytic activity towards ORR and OER, hierarchically arranged hollow porous architecture, high surface area and large pore volume. Such a structure is not only beneficial to expand active electrochemical sites and promote the electrolyte diffusion but also accommodates more discharge products when used as an air electrode material in LOBs. Fig. S5a† presents the initial full discharge/charge profiles of CuO–CuCo$_2$O$_4$- and pure Super P-based LOBs at 100 mA g^{-1}. The CuO–CuCo$_2$O$_4$ composite delivered an initial discharge capacity of 6844 mA h g^{-1} and presented a stable discharge plateau at ~2.79 V, whereas the pure Super P cathode delivered an initial capacity of 6054 mA h g^{-1} and exhibited a potential plateau at 2.65 V.

Furthermore, the discharge/charge overpotential of the CuO–CuCo$_2$O$_4$ cathode has been significantly reduced to 1.15 V, which confirms the superior catalytic activity of CuO–CuCo$_2$O$_4$ composite towards ORR and OER in non-aqueous LOBs. We also tested the full discharge/charge performance of pure Super P based- and CuO–CuCo$_2$O$_4$ based-electrodes under a voltage-limiting mode within 2.2–4.4 V without capacity limitation, as shown in Fig. S5b and c,† respectively. Due to the good reversibility, the CuO–CuCo$_2$O$_4$ based-electrode still delivered a high capacity over 1000 mA h g^{-1} after 7 cycles under a current density of 500 mA g^{-1} whereas the Super P based-electrode only show 1 cycles. The rate capability of LOBs, with two different cathodes, has been evaluated by carrying out discharge/charge testing at different current densities, ranging from 100 to 1000 mA g^{-1} (Fig. 5b). Although the discharge capacity of both cathodes decreased with increasing current density because of enhanced polarization, the discharge capacity of CuO–CuCo$_2$O$_4$ cathode remained higher than the discharge capacity of Super P cathode. At the current density of 200, 500 and 1000 mA g^{-1}, the CuO–CuCo$_2$O$_4$ composite cathode exhibited the discharge capacity of 5276, 4917 and 3903 mA h g^{-1}, whereas the Super P cathode delivered the capacity of 4556, 2943 and 1731 mA h g^{-1}, respectively. A comparative chart of average discharge specific capacities with error-bar was also provided to avoid the measurement errors, as given in Fig. S6.† Although the specific capacities vary from one to another when using coin-type cells, the trend that the synthesized catalyst can increase the discharge capacities is obvious and affirmatory. Moreover, it
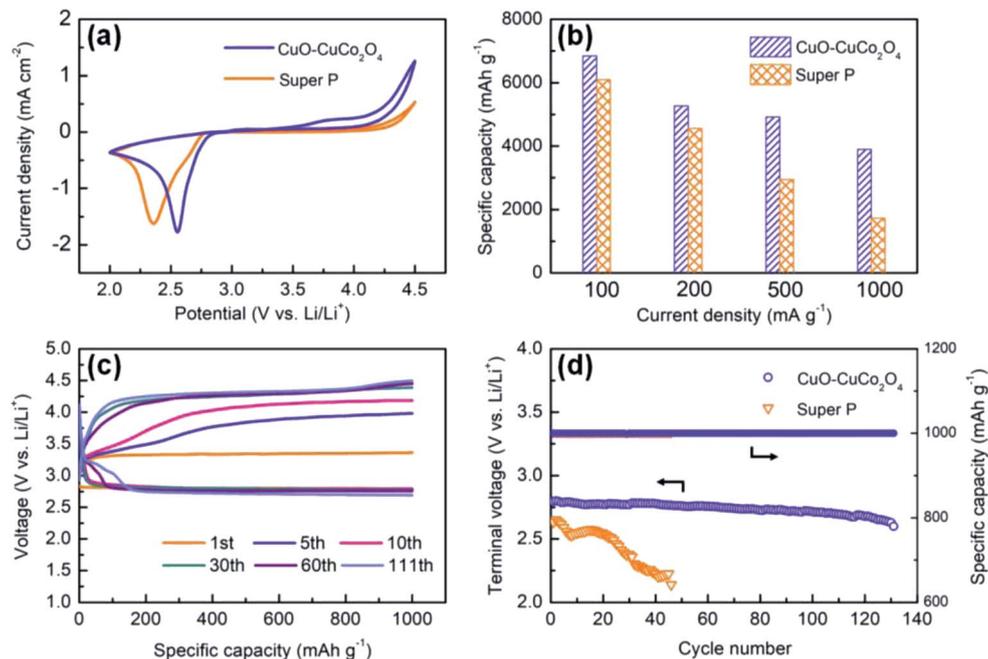
Fig. 5 Electrochemical characterization of CuO–CuCo$_2$O$_4$ and pure Super P-based LOBs: (a) CV profiles, (b) 1st cycle discharge capacity at different rates, (c) cyclic profiles of the CuO–CuCo$_2$O$_4$ based cathode at 400 mA g^{-1} with a capacity cut-off of 1000 mA h g^{-1}, and (d) cyclic performance and corresponding terminal discharge voltage.

can be readily observed that the CuO–CuCo$_2$O$_4$ composite cathode retained 74% of the initial capacity when the current density was enhanced from 200 to 1000 mA g^{-1}. However, the Super P cathode only retained 38% of the initial capacity with increasing current density, which confirms the superior rate performance of CuO–CuCo$_2$O$_4$ composite cathode.

Furthermore, the cyclic performance, which is a key performance criterion in LOBs, can be remarkably improved by employing a high-efficient catalyst. Herein, the cyclic performance of CuO–CuCo$_2$O$_4$ composite cathode and Super P cathode has been investigated by measuring the restricted capacity of 1000 mA h g^{-1} at 400 mA g^{-1} in the voltage range of 2.2 to 4.5 V, as shown in Fig. 5c and d. During the first cycling process, CuO–CuCo$_2$O$_4$ composite showed a high discharge potential of ~2.80 V, which is obviously higher than the Super P cathode (~2.65 V vs. Li/Li$^+$). Moreover, CuO–CuCo$_2$O$_4$ composite cathode demonstrated a low charging potential of ~3.34 V, which is 0.54 V higher than the discharge voltage and indicates the superior OER catalytic activity. The CuO–CuCo$_2$O$_4$ composite and Super P cathodes exhibited a cycling efficiency of 83.9% and 61.0% (discharge platform voltage/charge platform voltage), respectively. During the initial 10 cycles, the charging potential increased with increasing ohmic resistance due to the formation of solid electrolyte interface (SEI) film on the lithium metal and the partial deactivation of the active sites on the cathode surface.[5,29]

Furthermore, after 111 charge/discharge cycles, CuO–CuCo$_2$O$_4$ composite cathode maintained a high terminal discharge voltage of 2.69 V under the limited charge voltage of 4.5 V. On the other hand, the Super P cathode only remained operational for 46 charge/discharge cycles and the terminal discharge voltage quickly decreased to 2.14 V, as given in Fig. S5d.† The electrochemical performance of CuCo$_2$O$_4$ and other MOF-derived transition metal oxides in Li–O$_2$ batteries has been summarized in Table S1.† It can be readily observed that the as-synthesized CuO–CuCo$_2$O$_4$ composite delivered superior electrocatalytic performance than the previously reported MOF-derived transition metal oxides. The outstanding electrocatalytic performance of CuO–CuCo$_2$O$_4$ composite can be ascribed to the synergetic effect of intrinsic catalytic activity and the hollow porous dodecahedral architecture.

In addition, the ex situ XRD and SEM analysis were carried out to observe the structural and morphological changes in CuO–CuCo$_2$O$_4$ composite cathode during charging/discharging. Fig. 6a shows the coexistence of CuCo$_2$O$_4$ and Li$_2$O$_2$ after the 1st discharge state, which indicates that Li$_2$O$_2$ is the dominant product in the ORR process. However, the Li$_2$O$_2$ is fully decomposed after charging, which indicates the excellent reversibility of the discharge product during the charge–discharge process. Furthermore, the ex situ SEM images (Fig. 6c) show that the surface of CuO–CuCo$_2$O$_4$ cathode is entirely covered by insoluble flake-like reaction products after the discharge process, which is consistent with the reported morphology of Li$_2$O$_2$ discharge product.[30,31] However, the flake-like reaction product has been completely removed from the cathode surface after the charge process, as shown in Fig. 6d, preserving the initial cathode morphology (Fig. 6b). These observations confirm the excellent reversibility of the CuO–CuCo$_2$O$_4$ composite cathode.
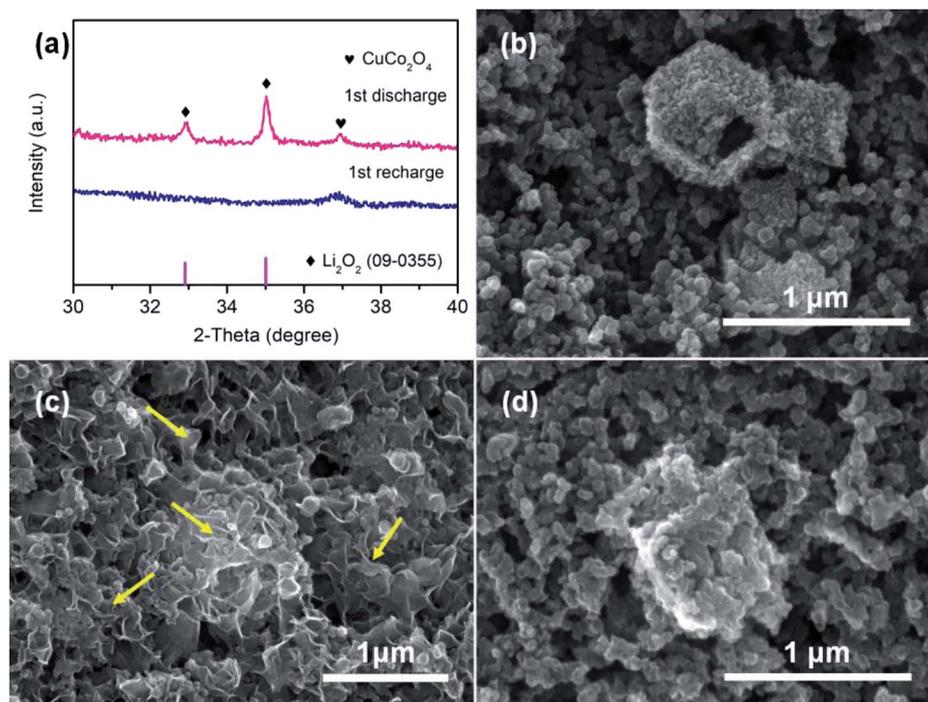
Fig. 6 Post-electrochemical material characterization: (a) *ex situ* XRD patterns and SEM images of the (b) pristine, (c) completely discharged (Li_2O_2 as shown by the yellow arrows), and (d) completely charged $CuO–CuCo_2O_4$ composite cathodes.

4. Conclusions

In all, we have proved the successful synthesis of MOF-derived $CuO–CuCo_2O_4$ composite by solvothermal method and used as a cathode catalyst in rechargeable LOBs. Owing to the unique morphology of ZIF–67 template, the as-synthesized $CuO–CuCo_2O_4$ composite rendered dodecahedron morphology with hollow porous structure. The hierarchically constructed meso- and macro-pores provided abundant electrocatalytic active sites and large surface area, which facilitated the charge transfer kinetics, resulted in efficient transportation of reactants/electrons and accommodated the discharge products, *i.e.*, Li_2O_2. Overall, the $CuO–CuCo_2O_4$ composite resulted in significantly enhanced electrocatalytic activity for ORR and OER in non-aqueous LOBs. As a result, the $CuO–CuCo_2O_4$ composite cathode delivered a high discharge capacity of 6844 mA h g^{-1} at 100 mA g^{-1} and stable cycle life up to 111 cycles. The flake-like Li_2O_2 discharge product and the excellent reversibility of the $CuO–CuCo_2O_4$ based air electrode were also revealed by *ex situ* XRD and SEM characterizations. These results reveal that MOF-derived $CuO–CuCo_2O_4$ composite is a promising cathode catalyst for high-performance and long-life LOBs.

Conflicts of interest

There are no conflicts to declare.

Acknowledgements

References

1 K. M. Abraham, *J. Phys. Chem. Lett.*, 2015, **6**, 830–844.
2 P. G. Bruce, S. A. Freunberger, L. J. Hardwick and J. M. Tarascon, *Nat. Mater.*, 2011, **11**, 19–29.
3 N. Akhtar and W. Akhtar, *Int. J. Energy Res.*, 2015, **39**, 303–316.
4 T. Vegge, J. M. Garcia-Lastra and D. J. Siegel, *Curr. Opin. Electrochem.*, 2017, **6**, 100–107.
5 H. Wu, W. Sun, Y. Wang, F. Wang, J. Liu, X. Yue, Z. Wang, J. Qiao, D. W. Rooney and K. Sun, *ACS Appl. Mater. Interfaces*, 2017, **9**, 12355–12365.
6 A. Chamaani, M. Safa, N. Chawla and B. El-Zahab, *ACS Appl. Mater. Interfaces*, 2017, **9**, 33819–33826.
7 J. Ren, Z. Huang, P. K. Kalambate, Y. Shen and Y. Huang, *RSC Adv.*, 2018, **8**, 28496–28502.
8 R. Bi, G. Liu, C. Zeng, X. Wang, L. Zhang and S. Z. Qiao, *Small*, 2019, **15**, e1804958.
9 N. Chawla, A. Chamaani, M. Safa and B. El-Zahab, *J. Electrochem. Soc.*, 2016, **164**, A6303–A6307.
10 J. Gao, X. Cai, J. Wang, M. Hou, L. Lai and L. Zhang, *Chem. Eng. J.*, 2018, **352**, 972–995.
11 H. Dong, P. Tang, S. Zhang, X. Xiao, C. Jin, Y. Gao, Y. Yin, B. Li and S. Yang, *RSC Adv.*, 2018, **8**, 3357–3363.
12 S. Liu, C. Wang, S. Dong, H. Hou, B. Wang, X. Wang, X. Chen and G. Cui, *RSC Adv.*, 2018, **8**, 27973–27978.
13 Y. Chen, D. Cao, S. Zhang, F. Yu and Y. Wu, *Batteries Supercaps*, 2019, **2**, 1–13.

14 T. Grewe, X. Deng, C. Weidenthaler, F. Schüth and H. Tüysüz, *Chem. Mater.*, 2013, **25**, 4926–4935.

15 H. T. Wu, W. Sun, J. R. Shen, Z. Mao, H. Wang, H. Q. Cai, Z. H. Wang and K. N. Sun, *ACS Sustainable Chem. Eng.*, 2018, **6**, 15180–15190.

16 S. Xu, Y. Yao, Y. Guo, X. Zeng, S. D. Lacey, H. Song, C. Chen, Y. Li, J. Dai, Y. Wang, Y. Chen, B. Liu, K. Fu, K. Amine, J. Lu and L. Hu, *Adv. Mater.*, 2018, **30**, 1704907.

17 Y. Li, Y. Xu, W. Yang, W. Shen, H. Xue and H. Pang, *Small*, 2018, **14**, e1704435.

18 M. Yuan, R. Wang, W. Fu, L. Lin, Z. Sun, X. Long, S. Zhang, C. Nan, G. Sun, H. Li and S. Ma, *ACS Appl. Mater. Interfaces*, 2019, **11**, 11403–11413.

19 C. Deng and D. W. Wang, *Batteries Supercaps*, 2019, **2**, 290–310.

20 J. Zhang, L. Wang, L. Xu, X. Ge, X. Zhao, M. Lai, Z. Liu and W. Chen, *Nanoscale*, 2015, **7**, 720–726.

21 W. Yin, Y. Shen, F. Zou, X. Hu, B. Chi and Y. Huang, *ACS Appl. Mater. Interfaces*, 2015, **7**, 4947–4954.

22 A. Li, X. Zhang, Z. Xie, Z. Chang, Z. Zhou and X. H. Bu, *Inorg. Chem.*, 2018, **57**, 14476–14479.

23 C. Sun, J. Yang, X. Rui, W. Zhang, Q. Yan, P. Chen, F. Huo, W. Huang and X. Dong, *J. Mater. Chem. A*, 2015, **3**, 8483–8488.

24 S. Xu, Y. Yao, Y. Guo, X. Zeng, S. D. Lacey, H. Song, C. Chen, Y. Li, J. Dai, Y. Wang, Y. Chen, B. Liu, K. Fu, K. Amine, J. Lu and L. Hu, *Adv. Mater.*, 2018, **30**, 1704907.

25 H. Kim, H. Lee, M. Kim, Y. Bae, W. Baek, K. Park, S. Park, T. Kim, H. Kwon, W. Choi, K. Kang, S. Kwon and D. Im, *Carbon*, 2017, **117**, 454–461.

26 A. La RosaToro, R. Berenguer, C. Quijada, F. Montilla, E. Morallón and J. L. Vázquez, *J. Phys. Chem. B*, 2006, **110**, 24021–24029.

27 W. Sun, Y. Wang, H. T. Wu, Z. H. Wang, D. Rooney and K. N. Sun, *Chem. Commun.*, 2017, **53**, 8711–8714.

28 P. F. Li, W. Sun, Q. Yu, P. Yang, J. S. Qiao, Z. H. Wang, D. Rooney and K. N. Sun, *Solid State Ionics*, 2016, **289**, 17–22.

29 Z. Sadighi, J. Liu, F. Ciucci and J. K. Kim, *Nanoscale*, 2018, **10**, 15588–15599.

30 B. Sun, X. Huang, S. Chen, P. Munroe and G. Wang, *Nano Lett.*, 2014, **14**, 3145–3152.

31 J. Cheng, M. Zhang, Y. Jiang, L. Zou, Y. Gong, B. Chi, J. Pu and L. Jian, *Electrochim. Acta*, 2016, **191**, 106–115.